Available online at www.sciencedirect.com

ScienceDirect

Ceramics International 42 (2016) 1234–1245

CERAMICS INTERNATIONAL

www.elsevier.com/locate/ceramint

Determination of strain, site occupancy, photoluminescent, and thermoluminescent-trapping parameters of Sm^{3+}-doped $NaSrB_5O_9$ microstructures

B. Ramesh[a], G. Devarajulu[a], B. Deva Prasad Raju[b], G. Bhaskar Kumar[c], G.R. Dillip[d,*], A.N. Banerjee[d,***], S.W. Joo[d,**]

[a]Department of Physics, Sri Venkateswara University, Tirupati 517502, India
[b]Department of Future Studies, Sri Venkateswara University, Tirupati 517502, India
[c]Department of Humanities and Sciences, Sri Venkateswara College of Science and Technology, Chittoor 517127, India
[d]School of Mechanical Engineering and Technology, Yeungnam University, Gyeongsan 712749, South Korea

Received 22 May 2015; received in revised form 6 September 2015; accepted 10 September 2015
Available online 25 September 2015

Abstract

Monoclinic $NaSrB_5O_9:Sm^{3+}$ phosphors were synthesized by a conventional solid-state reaction method in air. X-ray diffraction (XRD) and X-ray photoelectron spectroscopy (XPS) studies revealed that the Sm^{3+} ions preferably occupy Sr^{2+} cation sites in the $NaSrB_5O_9$ host lattice. The doping-dependent crystallite size and lattice strain on the X-ray peak broadening of the $NaSrB_5O_9:Sm^{3+}$ phosphor was determined by the Scherrer and Williamson–Hall (W–H) methods. Trigonally and tetrahedrally coordinated boron atoms in the phosphors were confirmed by confocal Raman analysis. Under near-UV excitation (402 nm), the $NaSrB_5O_9:Sm^{3+}$ phosphors emitted reddish-orange light at 604 nm that corresponds to the $^4G_{5/2}\rightarrow{}^6H_{7/2}$ transition. The concentration quenching mechanism between the two Sm^{3+} ions within the host was proved to be the dipole-dipole interaction, and the critical distance was found to be 22.29 Å. The fitted luminescence decay curves in terms of a second-order exponential model suggest that the Sm^{3+} ions possess two different kinds of environments in the host lattice, which was supported by XPS analysis. The defects acting as trapping centers were investigated by thermoluminescence glow curves. The γ-irradiated $NaSrB_5O_9:Sm^{3+}$ phosphors show two major dosimetric glow peaks centered at about 188.83 and 378.66 °C, indicating two different kinds of trapping centers in the phosphors.

Keywords: Borate phosphor; Strain analysis; X-ray photoelectron spectroscopy; Color purity; Trapping parameters

1. Introduction

Over the last few decades, there has been continuous growing interest in the investigation of the spectroscopic properties of rare-earth (RE) ions incorporated into different inorganic host matrices in terms of searching for new materials with applications in lasers, optical devices, sold state dosimeters, and so forth. Among inorganic materials, radiation-induced defects in borate material have received great attention for thermoluminescence dosimetric (TLD) applications because of their nearly tissue-equivalent absorption coefficient, high sensitivity, low cost, and ease of preparation [1–3]. To date, the thermoluminescence characteristic of borates has been studied, such as Tm^{3+}, Tb^{3+}, and Dy^{3+}-doped $Sr_2Mg(BO_3)_2$ [4], $NaSr_4(BO_3)_3:Ce^{3+}$ [5], and $KSr_4(BO_3)_3$:Ce [6]. Several phosphors have been used in various fields, such as ionizing radiation detection, dating in archeology, and clinical and environmental applications. Many efforts are being made either to develop new phosphors or to improve the existing ones.

For the selection of TLD phosphor, a suitable rare-earth ion as an activator is crucial for the preparation of luminescence materials.

*Corresponding author. Tel.: +82 53 810 4483.
**Corresponding author. Tel.: +82 53 810 2568.
***Corresponding author. Tel.: +82 53 810 2453.
E-mail addresses: dillip.ngr@gmail.com (G.R. Dillip), arghya@ynu.ac.kr, banerjee_arghya@hotmail.com (A.N. Banerjee), swjoo@yu.ac.kr (S.W. Joo).

http://dx.doi.org/10.1016/j.ceramint.2015.09.055
0272-8842/

Among various rare-earth ions, the Sm^{3+} ion was proven to be an excellent activator for many inorganic materials for producing reddish-orange light in the visible region due to its excited $^4G_{5/2}$ state to the ground states ^6H_J ($J=5/2$, 7/2, 9/2, 11/2) [7,8]. Studies on the luminescence properties of Sm^{3+}-doped inorganic host matrices include Ba_2SnO_4:Sm^{3+} [9], $Na_6CaP_2O_9$:Sm^{3+} [10], and $BaMoO_4$:Sm^{3+} [11] have been reported. Recently, Wu et al. synthesized a new sodium strontium pentaborate, $NaSrB_5O_9$, and reported refinement of the crystal structure that revealed a monoclinic structure of the synthesized borate [12]. There were two different kinds of Sr^{2+} positions in the $NaSrB_5O_9$ crystal with suitable radii that allow the substitution of rare-earth ion dopants such as Sm^{3+} ions.

Studies on sodium strontium pentaborate were already carried out in our group. In our earlier reports, the synthesis, structural, and optical properties of Eu^{3+} and Dy^{3+}-doped $NaSrB_5O_9$ phosphors were demonstrated for their use in the near-UV-excited white light-emitting diodes [13,14]. A wide variety of dopants that could be incorporated into the borates will provide a different environment to the dopant, leading to various tunable luminescence and thermoluminescence properties of the phosphors. However, the reports on the structural, cation site, optical, and thermoluminescence properties of the $NaSrB_5O_9$ host matrix are limited. Therefore, in the present investigation, we studied the structural parameters by estimating the strain values, site occupancy of dopant ions, and defect states of Sm^{3+}-doped $NaSrB_5O_9$ phosphor.

The aim of the present work is to explore the relation between the structural, luminescence, and trapping parameters of $NaSrB_5O_9$:Sm^{3+} phosphor. To the best of our knowledge, there are no reports on the structural and thermoluminescence properties of Sm^{3+}-doped $NaSrB_5O_9$ phosphor. The environment of dopant ions in the host matrix was investigated by correlating XPS, luminescence decay, and TL glow curves for the first time. Importantly, the trapping parameters such as trap depth (E) and frequency factor (s) were estimated by using Chen's peak shape method, which revealed information about the nature of the traps present in the Sm^{3+}-doped $NaSrB_5O_9$ phosphor. The results are highly useful for further research on the host matrix to understand its luminescence properties in detail.

2. Material synthesis

In a typical process, polycrystalline samples of undoped and Sm^{3+}-doped $NaSrB_5O_9$ phosphors were synthesized using a conventional solid-state reaction method. High-purity (99.99%) analytical grade (AR) starting materials Na_2CO_3, $SrCO_3$, H_3BO_3, and Sm_2O_3 were purchased from Sigma-Aldrich (USA) and used as received without further purification. The Sm^{3+}-dopant content was fixed at 0, 1, 3, 5, and 7 at% in the host matrix. For the synthesis of phosphor, stoichiometric quantities of starting materials were first calculated and mixed homogeneously in an agate mortar for 1 h. Afterward, each of the mixtures was kept in porcelain crucibles, gradually heated up to 800 °C in an electric furnace, and kept at this temperature for 8 h. Thereafter, the products were cooled down to room temperature (RT) in the furnace and finally ground again into fine powder for further measurements.

To identify the phase purity of the synthesized powders, powder X-ray diffraction measurements were carried out on an X-ray diffractometer (PANanalytical X'Pert PRO, USA) using *Cu* K_α radiation (0.154056 nm) at 40 kV and 30 mA. The data were collected between 10° and 80° with a step size of 0.02°. The morphology of the powder was examined by field emission scanning electron microscope (FE-SEM) (S-4200, Hitachi, Japan). An ultra-thin layer of platinum was sputter-coated (E-1030 Ion Sputter, Hitachi, Japan) on the powder sample surface to improve the conductivity during SEM measurement. Raman spectra of phosphors were obtained on a confocal Raman spectrometer (Labram HR 800, USA) using a Nd:YAG laser source with excitation at 532 nm, and the data were recorded in the range of 1400–800 cm^{-1}. X-ray photoelectron spectroscopy (XPS) analysis was carried out to investigate the surface properties of the phosphor using an X-ray photoelectron spectrometer (K-alpha, Thermo Scientific, USA). Monochromatic *Al* K_α X-ray radiation (1486.6 eV) was used as a source, and the data were recorded and processed using the commercial software Avantage (version 5.932, Thermo Scientific, USA). The low and high-resolution spectra were recorded using pass energies of 200 and 30 eV with step sizes of 1 eV and 0.1 eV, respectively. Using the software, the narrow scans were fitted to a Shirley-type background and then deconvoluted into various components using a GL30 program (a mixture of Gaussian (70%) and Lorentzian (30%)).

The optical properties of the phosphors were recorded on a UV–vis–NIR spectrophotometer (Jobin Varian Cary 5000, USA) in the reflectance mode. The data were collected in the range of 800–200 nm using polytetrafluoroethylene (PTFE) as a standard. The photoluminescence excitation, emission, and decay curve measurements were performed using a fluorimeter (Jobin Yvon Fluorolog-3, USA) with a xenon lamp as the excitation source. All the measurements were carried out at RT. Prior to thermoluminescence measurements, the powders were exposed to gamma (γ) rays using a ^{60}Co source at a rate of 0.322 kGy h^{-1} for 5 Gy. The exposure time was varied to 1, 5, 30, 90, and 180 min. After the desired exposure time, the glow curves were recorded immediately on a standard TL reader (Harshaw-3500, USA) in the range of RT to 400 °C at a heating rate of 5 °C/s. For comparison, commercially available $CaSO_4$:Dy was recorded at the same dose.

3. Results and discussion

3.1. X-ray diffraction studies

A comparison of XRD patterns of the $NaSrB_5O_9$:Sm^{3+} phosphors ($Sm^{3+}=0$–7 at%) to the standard XRD data of the $NaSrB_5O_9$ host matrix is shown in Fig. 1(a). The identified reflections for all samples were well indexed with the monoclinic crystal structure of $NaSrB_5O_9$ crystal reported by the standard Joint Committee on Powder Diffraction Standards – The International Centre for Diffraction Data (JCPDS-ICDD: 056-0415). Although significant reflections regarding Sm_2O_3

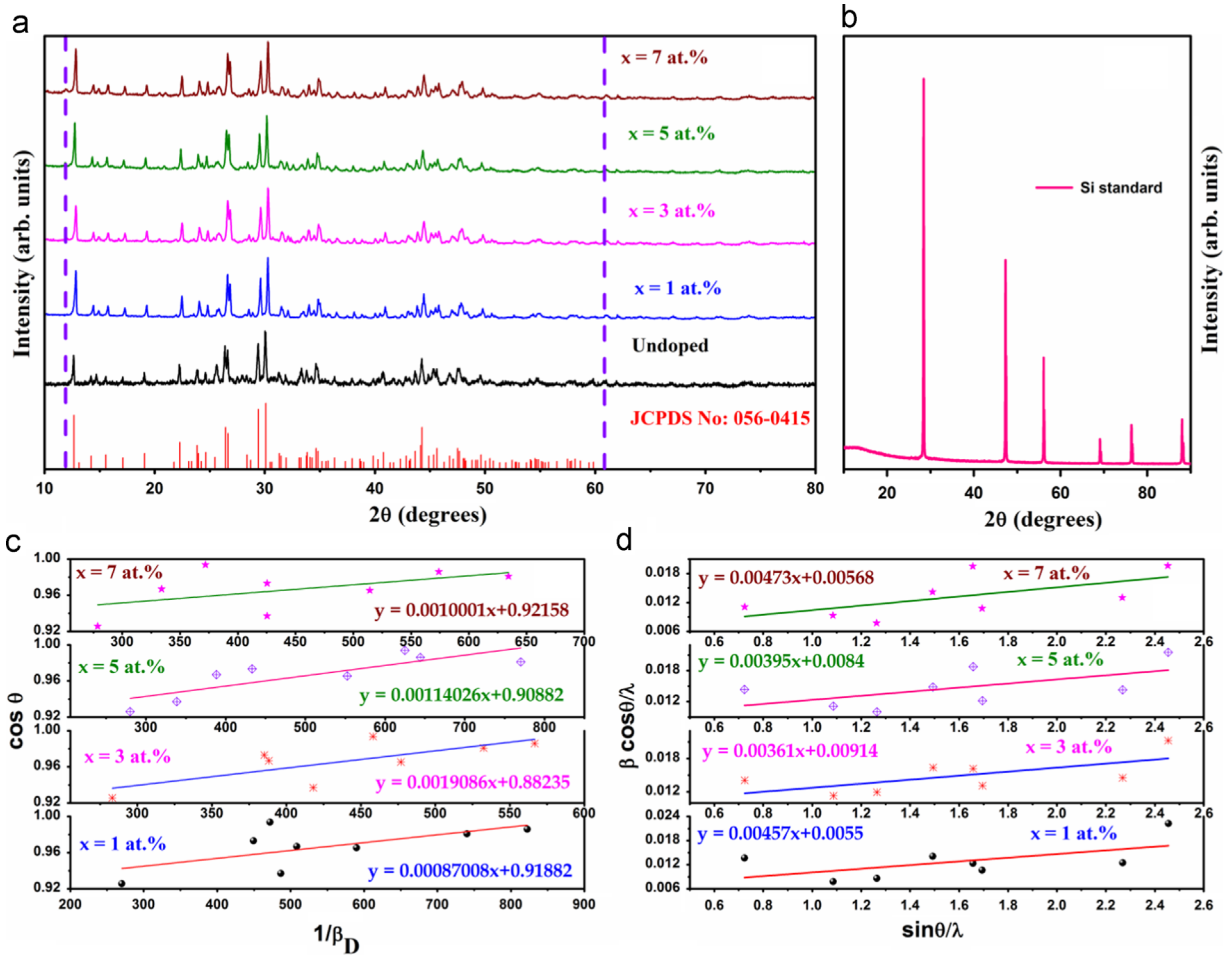

Fig. 1. (a) XRD patterns of $NaSr_{1-x}B_5O_9:Sm^{3+}_x$ phosphors (x=0–7 at%) and (b) standard Si substrate, (c) plot of cos θ versus $1/\beta_D$, and (d) the W–H analysis of $NaSr_{1-x}B_5O_9:Sm^{3+}_x$ phosphors (x=1–7 at%).

were not noticed in the XRD patterns, the dominant peaks were shifted towards higher 2θ angle due to the increase of Sm^{3+} ion concentration in the host. This is because the introduced Sm^{3+} ions might create strain within the crystal, which may displace the XRD peaks of phosphors from the mean position.

To identify the cation sites of the host to the dopant ions, the ionic radii of all cations ($Na^+/B^{3+}/Sr^{2+}$) were considered. The ionic radius of Na^+ is 1.02 Å (CN=6), that of Sr^{2+} is 1.26 Å (CN=8), that of B^{3+} is 0.11 Å (CN=4), and that of Sm^{3+} is 1.10 Å (CN=8) [15–17]. We believe that the Sm^{3+} ions are incorporated at the Na^+/Sr^{2+} cation sites in the host because of the similar ionic radii of both the ions. Therefore, a possible approach to obtain the charge compensation of the $NaSrB_5O_9:Sm^{3+}$ phosphor is through two Sm^{3+} ions substituting for three Sr^{2+} ions, which results in formation of two positive charge defects (Sm^0_{Sr}) and one negative defect (V''_{Sr}) (type-I), as well as one Sm^{3+} ion substituting for each of Sr^{2+} and Na^+ ion, which resulted in the formation of two positive charge defects (Sm^0_{Sr} and Sm^0_{Na}) (type-II). Thus, these processes could take place according to the following equations [18,19]:

$$2Sm^{3+} \rightarrow 3Sr^{2+} + 2Sm^0_{Sr} + V''_{Sr} \quad (type - I) \tag{1}$$

$$Sm^{3+} \rightarrow Sr^{2+} + Na^{+} + Sm^0_{(Sr/Na)} \quad (type - II) \tag{2}$$

However, the results of XPS analysis (Fig. 4(f)) show the presence of two states of Sm (Sm^{3+} and Sm^{2+}) in the narrow scan of the Sm 3d spectrum. In the current case, the analysis of charge compensation behavior is very complex. Hence, the authors considered the type-I process for charge compensation of the $NaSrB_5O_9:Sm^{3+}$ phosphor.

To estimate the strain values generated in the $NaSrB_5O_9:Sm^{3+}$ phosphors (Sm^{3+} = 1, 3, 5, and 7 at%), the X-ray peak broadening method was adopted. The Debye–Scherrer formula was used to determine the average crystallite size of the powders by the X-ray line broadening method using the following relation [20]:

$$D = \frac{k\lambda}{\beta_D \cos\theta}, \tag{3}$$

where D is the crystallite size (nm), λ is the wavelength of X-rays used for XRD measurements (0.154056 nm for *Cu* K_α radiation), k is the shape factor (0.9), θ is the peak position, and β_D is the peak width at half maximum intensity (in radians). The breadth result of the Bragg peak is a combination of both instrumental and sample-dependent effects. To determine the instrumental broadening, the diffraction pattern of a

standard material (silicon) was collected, as shown in Fig. 1(b). The instrument-corrected broadening (β_D) corresponding to each diffraction peak of the phosphors was estimated using the following equation [21,22]:

$$\beta_D = \left[(\beta_{hkl})^2_{\text{measured}} - (\beta_{hkl})^2_{\text{instrumental}} \right]^{1/2}$$
$$D = \frac{k\lambda}{\beta_D \cos\theta}$$
$$\cos\theta = \frac{k\lambda}{D}\left(\frac{1}{\beta_D}\right) \quad (4)$$

The plots of $\frac{1}{\beta_D}$ on the x-axis and $\cos\theta$ along the y-axis for phosphors were drawn by taking the preferred orientation peaks of each sample in the range of $2\theta = 10 - 80°$, as shown in Fig. 1(c). The slope of the linear fits of the figure is used to calculate the crystallite size D, and the estimated values are presented in Table 1.

The strain induced in the synthesized powders due to crystal imperfection and distortion was analyzed by the Williamson–Hall (W–H) method. The observed line breadth of the XRD peak is a combinatorial effect of Scherrer's size equation (particle size) and strain ($\varepsilon \approx \frac{\beta_s}{\tan\theta}$), which is given by [23]:

$$\beta_{hkl} = \beta_s + \beta_D = \left(\frac{k\lambda}{D\cos\theta}\right) + (4\varepsilon \tan\theta)$$

Finally,

$$\frac{\beta\cos\theta}{\lambda} = \left(\frac{k}{D}\right) + \left(\frac{\varepsilon \sin\theta}{\lambda}\right) \quad (5)$$

The plots of $\frac{\beta\cos\theta}{\lambda}$ versus $\frac{\sin\theta}{\lambda}$ of $NaSrB_5O_9:Sm^{3+}$ phosphors ($Sm^{3+} = 1$, 3, 5, and 7 at%) result in straight lines, as shown in Fig. 1(d). The strain and crystallite size were estimated from the slope and y-intercept of the fit of curves to the linear equation. The comparison of crystallite size and strain values by the Scherrer and W–H methods is presented in Table 1. The strain and size values do not follow a similar trend of either increasing or decreasing as a function of Sm^{3+} ion concentration. However, the crystallite sizes matched well with the obtained strain values. In general, the strain is liberated in bigger particles. The various sizes of the phosphors result in non-uniform strain values, as listed in the table. Usually, the solid-state reaction process produces various sizes of particles during the preparation, leading to non-uniform strain within the crystal.

Table 1
Comparison of crystallite size and strain values of $NaSr_{1-x}B_5O_9$: Sm^{3+}_x phosphors (x=1–7 at%) by Scherrer and W–H methods.

Sm^{3+} ion content in host (at%)	Scherrer method	Size-strain plot method	
	D (nm)	D (nm)	ε ($\times 10^{-4}$)
1	159.4	163.7	11.43
3	72.7	98.4	9.03
5	98.9	107.1	9.88
7	138.6	158.5	11.83

3.2. SEM analysis

Fig. 2 shows the surface morphology of the synthesized phosphor ($NaSrB_5O_9:Sm^{3+}$ = 3 at%). The phosphor is formed by irregular gains with various sizes. In general, the agglomeration of particles is high when the phosphor is synthesized by solid-state reaction under high calcination. However, the aggregation is much less in the present phosphors, suggesting these phosphors could be used for practical applications. A closer look at the image suggests that plate-like morphology of the phosphor in the micrometer dimension is obtained, and some of these plates appear to have monoclinic crystal structure (highlighted in the images (Fig. 2) by white circles). This is corroborated by the XRD data. In our previous investigation, similar morphologies were observed in $NaSrB_5O_9:Dy^{3+}$ phosphors [14]. However, in the present study, the particles have less agglomeration than the $NaSrB_5O_9:Dy^{3+}$ phosphors because of the presence of Sm^{3+} in the host matrix. Therefore, this type of defined morphology warrants considerable attention for lighting applications.

3.3. Raman analysis

In order to substantiate the presence of trigonally coordinated boron (BO_3) and tetrahedral boron (BO_4) groups in the structure of $NaSrB_5O_9:Sm^{3+}$ phosphors, Raman analysis was carried out. Fig. 3 shows the recorded Raman spectra of $NaSrB_5O_9:Sm^{3+}$ phosphors in the wavenumber range of 1400–800 cm^{-1}. No significant Raman peak shifting was observed due to the increase of dopant concentration in the host matrix. In general, eighter triagonal or tetrahedral coordinated boron atom are formed to the coordination polyhedron of the borates. The band at around 1072 cm^{-1} with a shoulder (1060 cm^{-1}) is attributed to the symmetric stretching vibrations of trigonal boron in the [BO_3] groups, whereas the band at 1309 cm^{-1} is due to the antisymmetric stretching modes of trigonal boron. The vibration near 1120 cm^{-1} corresponds to the asymmetric stretching vibrations of B–O

Fig. 2. SEM image of $NaSr_{1-x}B_5O_9:Sm^{3+}_x$ phosphor (x=3 at%).

bond in tetragonal coordinated borate groups [BO_4] [24–26]. The Raman analysis shows that the boron atoms in the $NaSrB_5O_9$:Sm^{3+} phosphors are trigonally and tetrahedrally coordinated to obtain the BO_3 and BO_4 groups.

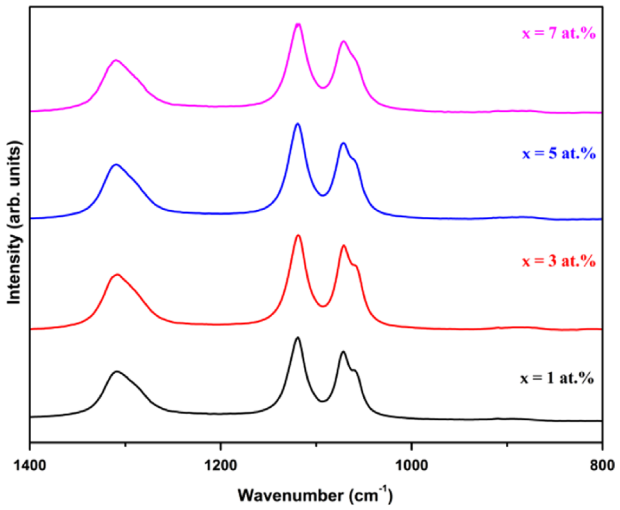

Fig. 3. Raman spectra of $NaSr_{1-x}B_5O_9$:Sm_x^{3+} phosphors (x=1–7 at%).

3.4. XPS analysis

To determine the chemical composition and the valence state of the elements in the Sm-doped $NaSrB_5O_9$ phosphors, XPS measurement was carried out. The wide scan spectrum of the $NaSrB_5O_9$:Sm^{3+} phosphor (Sm^{3+} = 3 at%) recorded in the range of 1350 to 0 eV is shown in Fig. 4(a). In the figure, surface elements such as B, C, O, Na, Sr, and Sm were noticed. The presence of carbon on the sample surface might be due to atmospheric carbon adsorbed on the surface during the preparation of the sample for measurement under non-vacuum conditions [27]. Therefore, in the present case, the C 1s high resolution spectrum was discarded.

To identify the valence states of the sample, the core level spectra of B 1s, O 1s, Na 1s, Sr 3d, and Sm 3d were recorded and deconvoluted using Avantage software, as shown in Fig. 4 (b–f), respectively. The asymmetric B 1s spectrum consists of two peaks at about 192.81 and 194.36 eV, which are assigned to the boron atoms bonded to oxygen atoms (B–O) in the host lattice and the adsorption of atmospheric hydroxyl groups on the sample surface during the preparation and/or incomplete decomposition of boric acid used for the preparation of the starting melts of $NaSrB_5O_9$ by solid-state reaction, respectively. The absence of a lower binding energy peak near

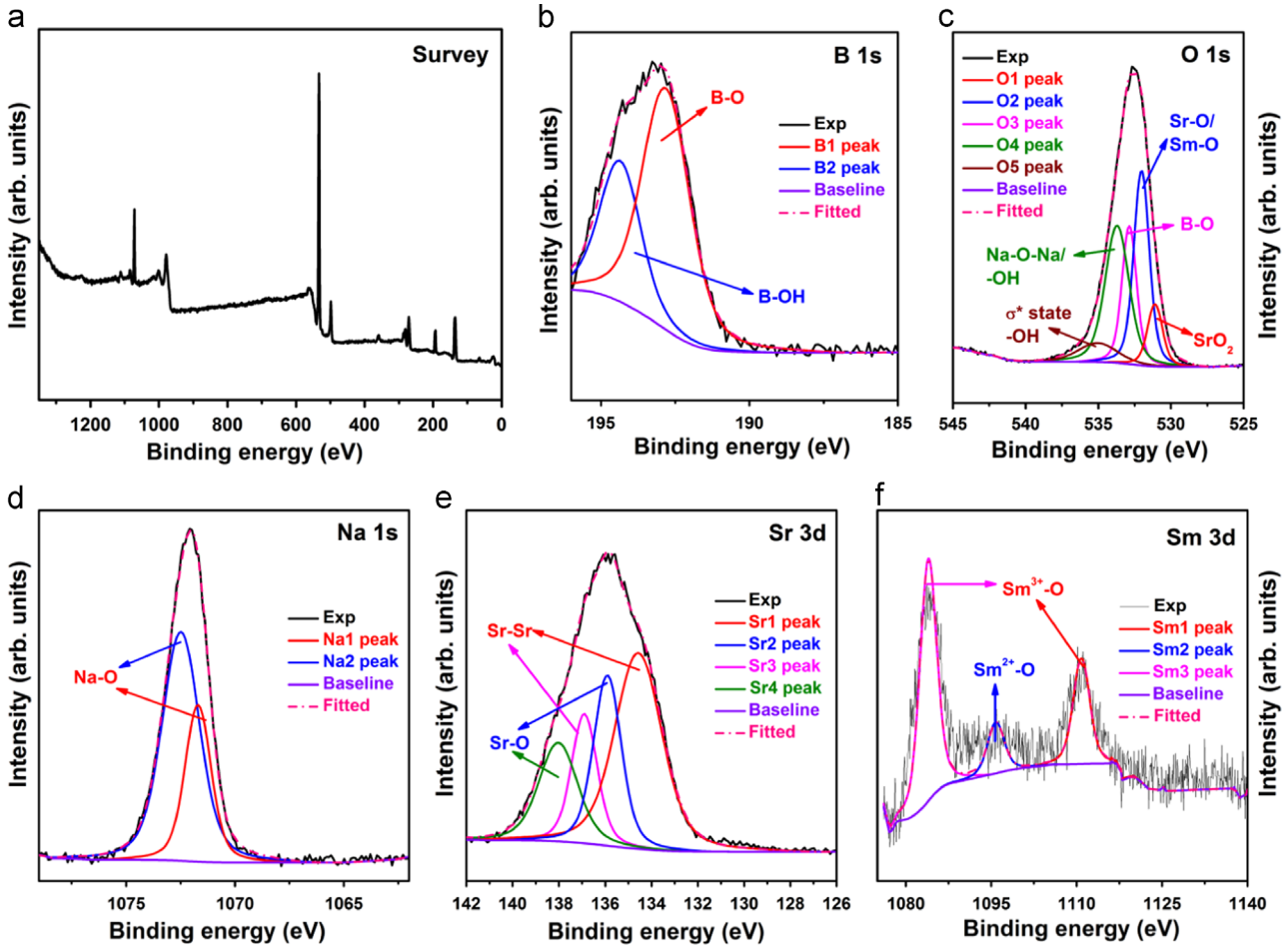

Fig. 4. (a–f) Wide and narrow scans of B 1s, O 1s, Na 1s, Sr 3d, and Sm 3d of $NaSr_{1-x}B_5O_9$:Sm_x^{3+} phosphor (x=3 at%), respectively.

191.2 eV indicated that the boron-to-carbon (B–C) bonding was not observed in the present case [28,29].

The O 1s high-resolution spectrum fitted into five components that correspond to various lattice sites of oxygen in the host matrix at around 531.1, 532.02, 532.87, 533.71, and 535.04 eV, which are attributed to the SrO_2, Sr–O, Sm–O, B–O, and π^* states of chemisorbed –O–H species, or partially to Na–O–Na bonding, and to the σ^* state of –OH from the hydroxyl groups [29–32]. The Na 1s spectrum was fitted to two peaks located at about 1071.9 and 1072.49 eV corresponding to Na–O bonds in the $NaSrB_5O_9$ phosphor. The bands are not observed at the lower binding energy near 1071.5 eV, indicating that the starting material Na_2CO_3 is completely decomposed by the solid-state reaction to form the host matrix with stoichiometric purity [33,34].

The high-resolution spectrum of Sr 3d is decomposed into four symmetrical peaks with the binding energies of 134.57, 135.91, 136.9, and 138.02 eV. This indicates that the Sr atoms in the $NaSrB_5O_9$:Sm^{3+} had two different environments. One was ascribed to the metallic Sr bonding (Sr–Sr) at about 134.57 and 136.9 eV for Sr $3d_{5/2}$ and $3d_{3/2}$, respectively. The other components at around 135.91 and 138.02 eV are due to the oxygen coordinated Sr atoms (Sr–O) in the host lattice for Sr $3d_{5/2}$ and $3d_{3/2}$, respectively [29,35].

The core-level spectrum of Sm 3d was deconvoluted into three sub-bands. The intense bands near 1083.95 and 1110.85 eV are due to the Sm-O bonds of Sm $3d_{5/2}$ and $3d_{3/2}$, respectively. The low-intensity peak centered at 1095.8 eV might be the Sm^{2+} component, indicating the presence of oxygen vacancies [36]. This confirms the co-existence of Sm^{2+} and Sm^{3+} states of Sm resulting two different chemical environments surrounding the samarium in the host matrix, which is corroborated by the decay profiles and TL glow curve analyses (Sections 3.7 and 3.9).

The atomic percentage of elements present in the $NaSrB_5O_9$:Sm^{3+} phosphor (3 at%) is listed in Table 2. The composition is close to the initial stoichiometric ratio, as mentioned in the experimental section, suggesting high purity of the synthesized sample. However, the stoichiometric percentage of strontium (Sr) is lower than that of sodium (Na), suggesting the possible substitution of Sm^{3+} ions at the Sr^{2+} sites instead of Na^+ sites in the host. The XPS analysis revealed the doping of Sm and the stoichiometric formation of Sm^{3+}-doped $NaSrB_5O_9$ phosphor.

Table 2
Atomic percentage variation of deconvoluted narrow scans of B 1s, O 1s, Na 1s, Sr 3d, and Sm 3d and their corresponding atomic weight percentage values.

Elemental peaks	Peak binding energy (eV)	Relative atomic concentration (%)	Elemental percentage (at%)
B1	192.81	21.57	32.14
B2	194.36	10.57	
O1	531.1	5.38	57.26
O2	532.02	17.34	
O3	532.87	11.6	
O4	533.71	18.67	
O5	535.04	4.27	
Na1	1071.9	1.85	5.73
Na2	1072.49	3.88	
Sr1	134.57	1.98	4.51
Sr2	135.91	1.01	
Sr3	136.9	0.71	
Sr4	138.02	0.81	
Sm1	1083.95	0.25	0.42
Sm2	1095.8	0.05	
Sm3	1110.85	0.12	

3.5. DRS analysis

Fig. 5(a) presents the DRS of $NaSrB_5O_9$:Sm^{3+} phosphors (Sm^{3+} = 1, 3, 5, and 7 at%). The strong absorption band centered at ~240 nm corresponds to the boron-to-oxygen (B–O) charge transition band (CTB) within the $NaSrB_5O_9$. This band is shifted towards the higher energy side (the lower wavelength region) with the increase of dopant concentration, which corroborates the XRD data [37]. A similar band was also observed in our previous reports for Eu^{3+} and Dy^{3+}-doped $NaSrB_5O_9$ phosphors [13,14]. In the range of 330–500 nm, as expected, several absorption bands were observed because of the presence of Sm^{3+} ions in the host matrix. These bands become stronger due to the increase of Sm^{3+} ions. The characteristic intense bands identified at about 344, 361, 375, 402, 422, 440, 461, 468, and 488 nm correspond to the ground state of $^6H_{5/2}$ to excited levels of $^4H_{13/2}$, $^4D_{3/2}$, $^6P_{7/2}$, $^4F_{7/2}$, $^6P_{5/2}$, $^4G_{9/2}$, $^4I_{9/2}$, $^4I_{11/2}$, and $^4I_{13/2}$, respectively [38]. Similar bands are also obtained in the excitation spectra of $NaSrB_5O_9$:Sm^{3+} phosphors (Section 3.6). Among the bands, the sharp peak at 402 nm is the strongest and useful for near-UV excitation applications, and hence it warrants considerable attention.

3.6. Photoluminescence studies

The excitation spectra of $NaSrB_5O_9$:Sm^{3+} phosphors (Sm^{3+} = 1–7 at%) were recorded under the emission wavelength of 604 nm and are shown in Fig. 5(b). The spectra are composed of several intense and sharp peaks and correspond to the *f–f* transition of the samarium ground state ($^6H_{5/2}$) to various excited states. The bands are located at around 343 nm ($^4H_{13/2}$), 361 nm ($^4D_{3/2}$), 373 nm ($^6P_{7/2}$), 402 nm ($^4F_{7/2}$), 422 nm ($^6P_{5/2}$), 441 nm ($^4G_{9/2}$), 461 nm ($^4I_{9/2}$), 469 nm ($^4I_{11/2}$), and 490 nm ($^4I_{13/2}$), which are consistent with the DRS peaks [8]. Within sharp lines, the dominant intense peak at 402 nm ($^6H_{5/2} \rightarrow {}^4F_{7/2}$) is used to measure the emission spectra of $NaSrB_5O_9$:Sm^{3+} phosphors. Thus, the excitation peak obtained at 402 nm suggests that the present phosphors are effectively excited by near-UV radiation, which can be used as a potential phosphor for UV/NUV LEDs.

Fig. 5(c) shows the photoluminescence emission spectra of the $NaSrB_5O_9$:Sm^{3+} phosphors (Sm^{3+} = 1, 3, 5 and 7 at%) recorded by the excitation of Sm^{3+} at 402 nm. The spectra have similar profiles, and no significant shift in peak position was observed for all concentrations of Sm^{3+} ions. In the wavelength range of 550–670 nm, the spectra consist of several sharp peaks related to *f–f* transition of Sm^{3+} ions

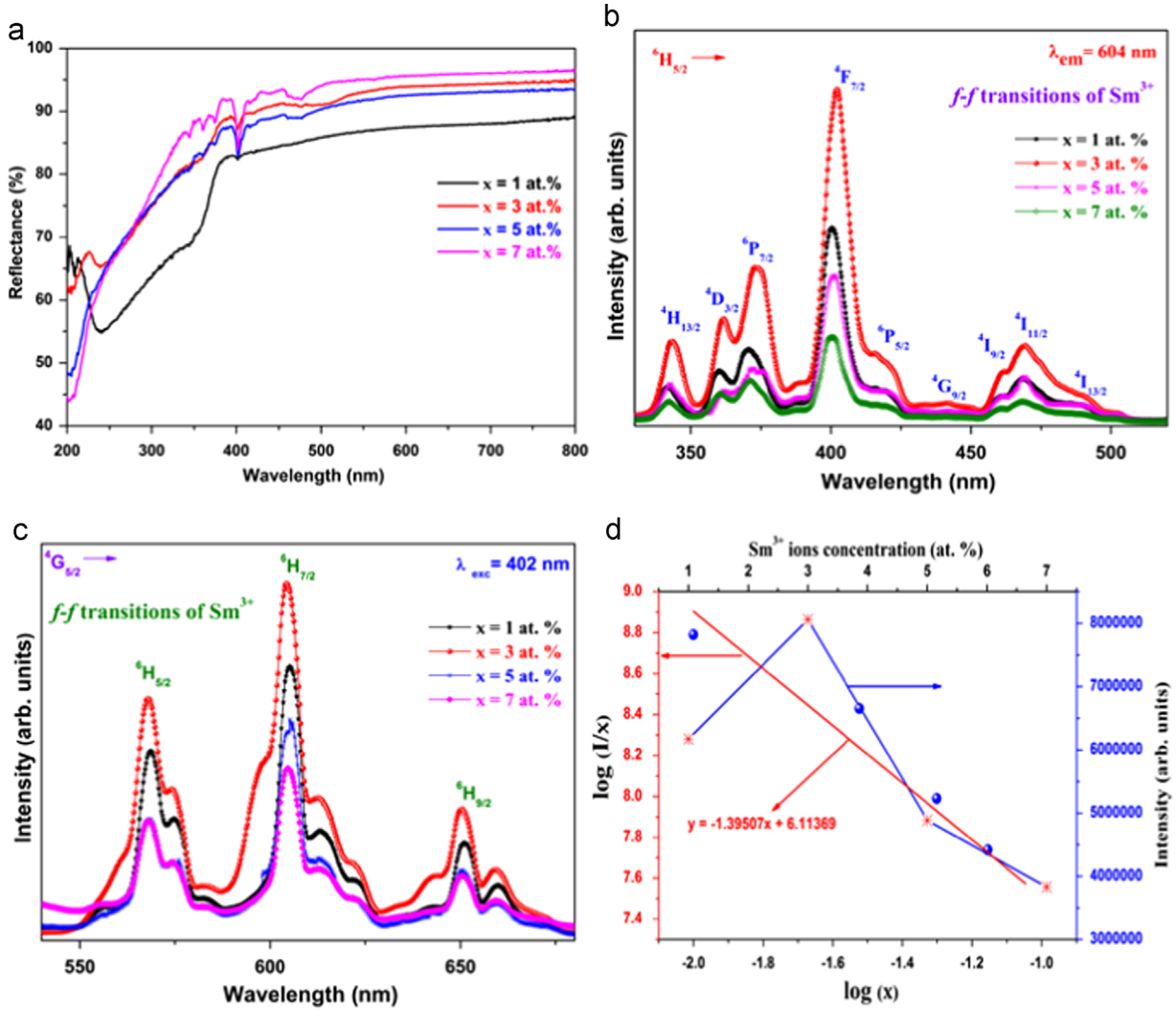

Fig. 5. (a) Diffuse reflectance spectra, (b) excitation spectra, (c) emission spectra of $NaSr_{1-x}B_5O_9:Sm^{3+}_x$ phosphors (x=1–7 at%), and (d) plot of log (I/x) versus log (x) (left) and the variation of emission intensity as a function of Sm^{3+} ions concentrations (right).

from the excited $^4G_{5/2}$ to different lower levels at around 568 nm ($^4G_{5/2}\rightarrow{}^6H_{5/2}$), 604 nm ($^4G_{5/2}\rightarrow{}^6H_{7/2}$), and 650 nm ($^4G_{5/2}\rightarrow{}^6H_{9/2}$).

The crystal field splitting of all three transitions is observed at about 574, 613, and 660 nm for $^4G_{5/2}\rightarrow{}^6H_{5/2}$, $^6H_{7/2}$, and $^6H_{9/2}$, respectively [39]. The strongest red emitting transition at 604 nm ($^4G_{5/2}\rightarrow{}^6H_{7/2}$) is a combinatorial effect of a partly magnetic dipole (MD) and partly electric dipole transition (ED) nature of the Sm^{3+} ions. The other transitions at 568 nm ($^4G_{5/2}\rightarrow{}^6H_{5/2}$) and 650 nm ($^4G_{5/2}\rightarrow{}^6H_{9/2}$) are purely MD and ED transitions, respectively, which could be sensitive to the crystal field strength around Sm^{3+} ions. In general, the intensity ratio of these two transitions has been used to measure the symmetric nature of trivalent 4*f* ions. A greater value of MD transition indicates more symmetric nature of Sm^{3+} ions in the crystal field [17]. In the present investigation, the integrated intensity ratio of MD-to-ED transition is greater than one, suggesting symmetric nature of the $NaSrB_5O_9$ host.

To investigate the effect of Sm^{3+} ion concentration on the emission intensity of the phosphors, the Sm^{3+} ion content was systematically varied in the host, as described in the experimental section. The emission intensity is increased with the Sm^{3+} ions concentration from 1 to 3 at%, and beyond that, the intensity is decreased due to the increase of dopant concentration. Thus, the optimum concentration of dopant is 3 at% in the host matrix. This is because of the concentration quenching of Sm^{3+} emission in the host matrix, which is the strong interaction that occurs between activation ions with reduced distance.

The emission intensity of the $NaSrB_5O_9:Sm^{3+}$ phosphor was decreased after 3 at% Sm^{3+} ions due to the non-radiative energy transfer between luminescent centers before being emitted. To further estimate the critical energy transfer distance (R_c) between the donors (activators) and acceptors (quenching sites) in the host, the following equation from Blasse was used [40]:

$$R_C \approx 2\left[\frac{3V}{4\pi x_c N}\right]^{1/3} \quad (6)$$

where V is the volume of the unit cell (Å^3), x_c is the critical concentration of dopant ions (at%), and N is the number of host cations (Sr^{2+}) in the unit cell. The estimated values of V,

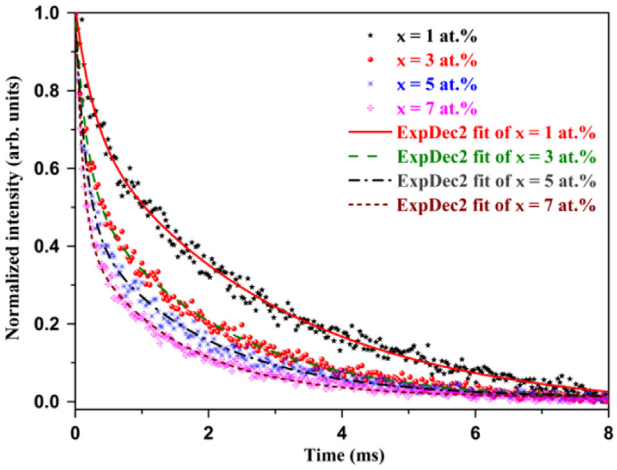

Fig. 6. Decay curves and second order exponential fit of $NaSr_{1-x}B_5O_9:Sm^{3+}_x$ phosphors (x=1–7 at%).

x_c, and N are 696.29 Å^3, 0.03, and 4, respectively. Therefore, the calculated critical distance between the activators (Sm^{3+}) in the $NaSrB_5O_9$ is found to be ~22.29 Å.

According to Dexter's theory, in many inorganic materials, the concentration quenching will usually occur due to the electric/magnetic multipolar interaction among similar activator ions in the host. The mechanism of interaction between Sm^{3+} ions in the $NaSrB_5O_9$ host could be expressed using the following relation [41]:

$$\frac{I}{x} = k\left[1 + \beta(x)^{\theta/d}\right]^{-1} \quad (7)$$

where I is the emission intensity, x is the activator concentration, d is the sample dimension (equal to 3 for energy transfer among the activators inside particles), k and β are constants for each interaction for a given host lattice (independent of activator concentration), and θ is the multipole index. θ values of 6, 8, and 10 correspond to the dipole–dipole (d–d), dipole–quadrupole (d–q), and quadrupole–quadrupole (q–q) interactions, respectively, and θ=3 for exchange interactions. Fig. 5 (d) gives a plot of log $(\frac{I}{x})$ versus log (x) at 604 nm emission. As shown in the figure, the linear fit of the plot gives a y-intercept of ~6.113 and a slope $(-\theta/3)$ of −1.395, yielding a θ of ~4.185, which is close to 6. Therefore, the results indicate that the non-radiative transition between the Sm^{3+} ions occurs through dipole-dipole interaction for the concentration quenching of Sm^{3+} in the $NaSrB_5O_9$ host.

3.7. Decay curve measurements

To further describe the concentration quenching in more detail, the decay curves were recorded and are shown in Fig. 6 for $NaSrB_5O_9:Sm^{3+}$ phosphors (Sm^{3+} = 1, 3, 5, and 7 at%). The profiles were collected for emission at 604 nm ($^4G_{5/2} \rightarrow {}^6H_{7/2}$) under an excitation wavelength of 402 nm. For all concentrations, the decay curves could be well fitted by a second-order exponential function according to the following relation [42]:

Table 3
Lifetimes, CIE, and color purity values of $NaSrB_5O_9:Sm^{3+}$ phosphors as a function of Sm^{3+} concentration.

Sm^{3+} concentration in host (at%)	Lifetimes (ms)	CIE values		Color purity (%)
		x	y	
1	2.87	0.552	0.442	98.93
3	1.90	0.565	0.432	99.17
5	1.60	0.534	0.452	97.02
7	1.31	0.523	0.459	96.98

$$I(t) = I(0) + A_1\exp\left(-t/\tau_1\right) + A_2\exp\left(-t/\tau_2\right) \quad (8)$$

where $I(0)$ and $I(t)$ are the emission intensity at time 0 and t, A_1 and A_2 are the fitting parameter, and τ_1 and τ_2 are the lifetimes, respectively. The effective lifetimes (τ) could be estimated using the following equation:

$$\tau = \left(A_1\tau_1^2 + A_2\tau_2^2\right)/\left(A_1\tau_1 + A_2\tau_2\right) \quad (9)$$

The fitted curves are shown in the figure as solid lines, and the calculated values are listed in Table 3. As expected, the lifetimes are decreased from 2.87 ms to 1.31 ms with the increase of Sm^{3+} concentration due to the energy transfer between the similar dopant ions. In general, the decay curves could be influenced by the energy transfer in the host material and are a good indicator for the number sites available to be occupied by dopant ions. All the curves exhibit second-order exponential behavior that indicates the co-existence of two site occupancies of Sm^{3+} in the host cation sites of Sr^{2+}. Similar results are also observed in the XPS spectrum of Sm 3d. Therefore, in the $NaSrB_5O_9:Sm^{3+}$ phosphors, the Sm^{3+} ions occupy the two different sites of Sr^{2+}.

3.8. Chromaticity coordinates and color purity

The CIE 1931 chromaticity coordinates were estimated using CIE calculation software to analyze the potentiality of the synthesized phosphors. The CIE diagram of $NaSrB_5O_9:Sm^{3+}$ phosphors (Sm^{3+} = 1, 3, 5, and 7 at%) is shown in Fig. 7. The estimated CIE coordinates are located in the orange–yellow region for all concentrations of Sm^{3+} ions. The color coordinates lie in the same region when the emission profiles are identical. The emission spectra are similar in nature for all samples except for the variations of intensity, as shown in Fig. 5(c). The CIE values of $NaSrB_5O_9:Sm^{3+}$ phosphors (Sm^{3+} = 1, 3, 5, and 7 at%) are tabulated in Table 3.

The color saturation or color purity values are calculated using the CIE diagram from the following relation [43]:

$$\text{Color purity} = \frac{\sqrt{(x-x_i)^2 + (y-y_i)^2}}{\sqrt{(x_d-x_i)^2 + (y_d-y_i)^2}} \times 100\% \quad (10)$$

where (x, y) and (x_i, y_i) are the chromaticity coordinates of the emission light and the CIE white light illumination (0.33, 0.33), respectively, and (x_d, y_d) are the color coordinates of the dominant wavelength points. The estimated color purity of the

$NaSrB_5O_9:Sm^{3+}$ phosphors ($Sm^{3+}=1$, 3, 5, and 7 at%) are presented in Table 3. The obtained values show better color purity near 99.17%.

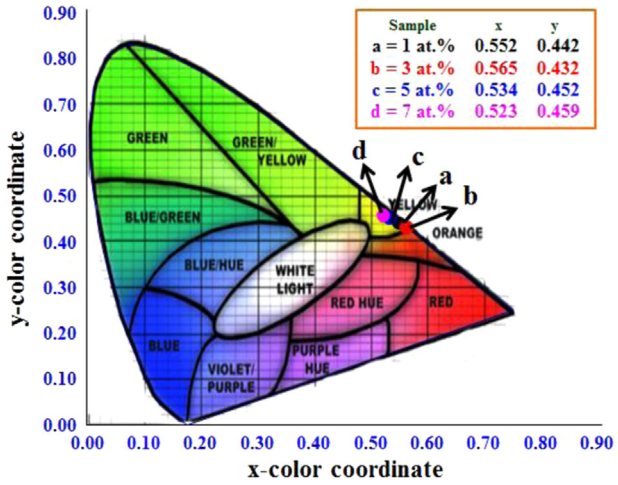

Fig. 7. CIE chromaticity diagram of $NaSr_{1-x}B_5O_9:Sm_x^{3+}$ phosphors ($x=1$–7 at%). (For interpretation of the references to color in this figure, the reader is referred to the web version of this article.)

3.9. Thermoluminescence properties

In order to study the defect properties of $NaSrB_5O_9:Sm^{3+}$ phosphors ($Sm^{3+}=1$, 3, 5, and 7 at%), the thermoluminescence (TL) glow curves were recorded. TL glow curves of the phosphors were collected using a ^{60}Co γ-ray irradiation source at a dose of 0.322 KGy h^{-1} for 5 Gy with irradiation times of 30 and 180 min, respectively, as shown in Fig. 8(a) and (b). The TL glow curve of commercially available $CaSO_4$:Dy is also shown in Fig. 8(a) with the same energy. The two glow curves were obtained for all concentrations with intensity variation. The two peaks are located at about 188.83 and 378.66 °C at a heating rate of 5 °C/sec. The results indicate that two different kinds of trapping/luminescence centers are created in the phosphors due to the irradiation of γ-rays.

The intensity of the glow curves decreased due to the increase of Sm^{3+} ion concentrations because of concentration quenching. Thus, the 1 at% Sm^{3+}-doped $NaSrB_5O_9$ showed the most efficient TL response. Moreover, the TL glow curves were recorded by varying the irradiation times to 1, 5, 30, 90, and 180 min. A typical TL glow curve of 1 at% Sm^{3+}-doped $NaSrB_5O_9$ phosphor as a function of irradiation time is shown

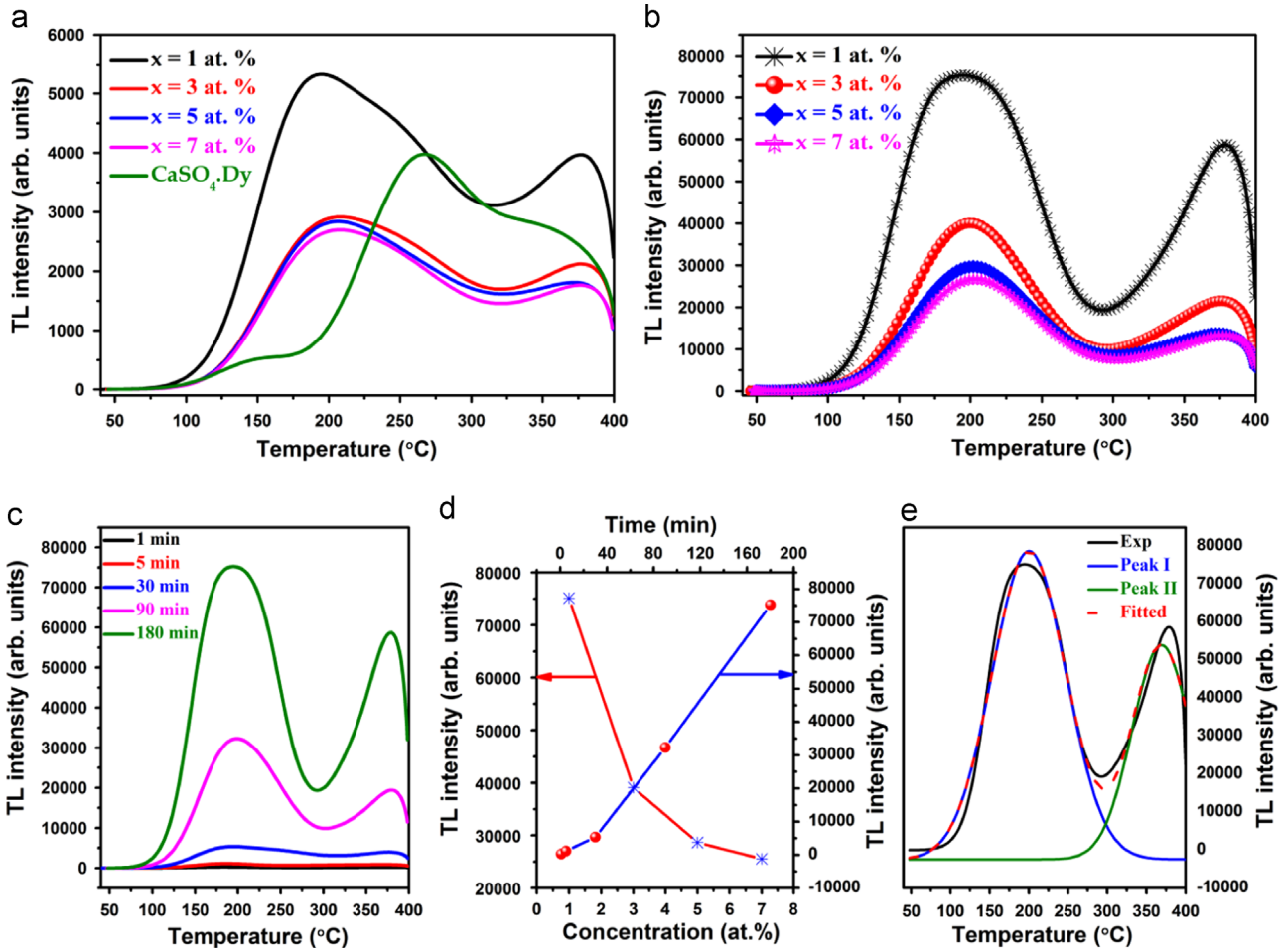

Fig. 8. (a and b) TL glow curves of $NaSr_{1-x}B_5O_9:Sm_x^{3+}$ phosphors ($x=1$–7 at%) with irradiation times of 30 and 180 min, respectively, (b) variation of TL intensity as a function of irradiation time of $NaSr_{1-x}B_5O_9:Sm_x^{3+}$ phosphor ($x=1$ at%), (d) variation of TL intensity with Sm^{3+} ion concentration at irradiation time of 180 min (left) and irradiation time (right), respectively, and (e) typical Gaussian fit of TL curve of $NaSr_{1-x}B_5O_9:Sm_x^{3+}$ phosphor ($x=1$ at%) at the irradiation time of 180 min.

in Fig. 8(c). Due to the increase of irradiation time, the intensity of the glow curve increases with similar profiles. The variation of TL intensity as a function of Sm^{3+} ion concentration and irradiation time is shown in Fig. 8(d).

The potential of any phosphor to be utilized as a thermoluminescence dosimetric phosphor mainly depends on the kinetic parameters of its glow peak, such as the order of kinetics (b) of the TL process, activation energy (E) for the TL traps, and frequency factor (s). Several methods were introduced to calculate the kinetic parameters of the glow curve, like various heating rate methods, the peak shape method, initial rise method, isothermal decay method, and glow curve deconvolution method [44,45]. In the current case, the TL glow curves were analyzed using Chen's peak shape method. The parameters affecting the kinetics such as the geometrical reproducibility and problem of contact of a sample with the heating planchet are eliminated by using Chen's peak shape method [46].

According to Chen's full width method, the geometrical factor μ_g of a TL peak is determined by the following equation:

$$\mu_g = \frac{\delta}{\varepsilon} = \frac{(T_2 - T_m)}{(T_2 - T_1)} \tag{11}$$

where T_1, T_2, and T_m are the temperature of half-intensity on the low temperature side, the high temperature side, and the peak temperature of the TL peak, respectively. The TL glow curves were deconvoluted using a Gaussian function, and the typical Gaussian fit of $NaSrB_5O_9:Sm^{3+}$ ($Sm^{3+} = 1$ at%) at an irradiation time of 180 min is shown in Fig. 8(e).

Chen's method is applied to the two fitted peaks to obtain the symmetry factor, μ_g. The value of μ_g is 0.42 and 0.52 for first- and second-order kinetics, respectively. Using the equation, the order of the kinetics is obtained, and the estimated values are presented in Table 4. The geometrical factor values exhibit second-order and first-order kinetics for the high-intensity peaks (peak-I) and a low-intensity peak (peak-II), respectively, for all concentrations of Sm^{3+} ions. The activation energy or trap depth E (eV) and frequency factor s (s^{-1}) could be calculated using the relation formulated by Chen, which is applicable for any order of kinetics:

$$\left.\begin{aligned} E &= C_\eta\left(kT_m^2/\eta\right) - b_\eta\left(2kT_m\right) \\ s &= \frac{\beta E}{kT_m^2}\exp\left(\frac{E}{kT_m}\right)\left[1 + (b-1)\Delta_m\right]^{-1} \\ C_\tau &= 1.51 + 3\left(\mu_g - \Delta\right) \\ C_\delta &= 0.976 + 7.3\left(\mu_g - \Delta\right) \\ C_\omega &= 2.52 + 10.2\left(\mu_g - \Delta\right) \\ b_\tau &= 1.58 + 4.2\left(\mu_g - \Delta\right) \\ b_\delta &= 0 \\ b_\omega &= 1 \end{aligned}\right\} \quad \text{and } \Delta_m = \frac{2kT_m}{E} \tag{12}$$

where η stands for τ, δ, and ω, while k is Boltzmann's constant, β is the heating rate (5 °C/s), and $\Delta = 0.42$ and 0.52 for first- and second-order TL peaks, respectively [5,47,48]. Using these equations, the activation energy (E) and frequency factor (s) were estimated and are summarized in Table 4. The first glow peak at 188.83 °C shows lower E and s values compared to the second glow peak at 378.66 °C, indicating the surface traps of the phosphor. Therefore, the second peak (378.66 °C) was due to deeper traps created during γ-irradiation. The E and s values of peaks I/II were 0.468/1.082 eV and $1.97\times10^6/1.42\times10^{10}$ s^{-1}, respectively, for 1 at% Sm^{3+} ions in the $NaSrB_5O_9$ phosphor.

4. Conclusion

$NaSrB_5O_9:Sm^{3+}$ phosphors have been synthesized using a facile one-step solid-state reaction method by sintering the samples at 800 °C in air. The average crystallite size of the phosphors was estimated to be in the range of 70–165 nm by Debye–Scherrer's equation and W–H analyses. The SEM image revealed plate-like morphology of the phosphor in the

Table 4
Trapping parameters from Chen's peak shape method in Sm^{3+}-doped $NaSrB_5O_9$ phosphors with ^{60}Co γ-ray irradiation source at the rate of 0.322 kGy h^{-1} for 5 Gy.

Sm^{3+} ion (at%)	Peak	T_1 (K)	T_2 (K)	T_m (K)	b	Trap depth (E) (eV)				Frequency factor (s) (s^{-1})			s_{mean}
						E_τ	E_δ	E_ω	E_{mean}	s_τ	s_δ	s_ω	
1	I	417.25	519.75	461.83	2	0.537	0.414	0.454	0.468	5.19E06	1.92E05	5.36E05	1.97E06
	II	617.67	669.53	651.65	1	1.242	0.877	1.126	1.082	3.82E10	4.10E07	4.41E09	1.42E10
3	I	428.35	515.66	470.3	2	0.557	0.408	0.468	0.478	6.69E06	1.32E05	6.03E05	2.48E06
	II	610.96	669.17	650.38	1	0.995	0.516	0.845	0.785	3.91E08	3.99E04	2.28E07	1.38E08
5	I	428.45	519.56	472.74	2	0.521	0.383	0.438	0.447	2.39E06	6.21E04	2.49E05	9.01E05
	II	611.45	669.65	649.8	1	1.068	0.732	0.960	0.920	1.57E09	2.70E06	2.05E08	5.93E08
7	I	426.23	520.34	474.58	2	0.447	0.309	0.366	0.374	3.09E05	7.91E03	3.38E04	1.17E05
	II	616.6	669.79	651.65	1	1.187	0.800	1.064	1.017	1.38E10	9.45E06	1.39E09	5.07E09

monoclinic crystal structure. The XPS results showed the B–O, Sr–O, Na–O, and Sm–O-related bonding information on the surface of the $NaSrB_5O_9:Sm^{3+}$ phosphor. Importantly, the stoichiometric formation of the $NaSrB_5O_9:Sm^{3+}$ phosphor was confirmed by XPS. With the excitation wavelength of 402 nm, the phosphors showed a strong reddish-orange emission at 604 nm ($^4G_{5/2} \rightarrow {}^6H_{7/2}$) with transition of the characteristic Sm^{3+} ions. A high color purity of 99.17% was achieved for the system. All the decay curves were well fitted to the second-order exponential equation, suggesting two different environments surrounding the Sm^{3+} ions in the host. The TL glow curves show two different kinds of trap centers in the phosphors created by the γ-ray irradiation. The mean trap depth (E) and frequency factor (s) of peaks I/II obtained by Chen's peak shape method are 0.468/1.082 eV and 1.97×10^6 /1.42×10^{10} s^{-1}, respectively. In conclusion, the plate-like morphology with defined structure and the diverse fluorescent and thermoluminescent properties of the proposed phosphor could lead to special interest for thermoluminescence dosimetric applications.

Acknowledgements

B. Deva Prasad Raju is thankful to the Department of Science and Technology of the Government of India for providing financial assistance in the form of a Major Research Project (Fast Track Research Project Young Scientist Award); vide reference no: DST-SR/FTP/PS-198/2012; dated:14-02-2014.

References

[1] S.W.S. Mckeever, Thermoluminescence of Solids, Cambridge University Press, Cambridge, England, 1985.
[2] C. Furetta, M. Prokic, R. Salamon, V. Prokic, G. Kitis, Dosimetric characteristics of tissue equivalent thermoluminescent solid TL detectors based on lithium borate, Nucl. Instrum. Methods Phys. Res. A 456 (2001) 411–417.
[3] L.H. Jiang, Y.L. Zhang, C.Y. Li, J.Q. Hao, Q. Su, Thermoluminescence properties of Ce^{3+}-doped $LiSr_4(BO_3)_3$ phosphor, Mater. Lett. 61 (2007) 5107–5109.
[4] L.Y. Liu, Y.L. Zhang, J.Q. Hao, C.Y. Li, Q. Tang, C.X. Zhang, Q. Su, Thermoluminescence studies of rare earth doped $Sr_2Mg(BO_3)_2$ phosphor, Mater. Lett. 60 (2006) 639–642.
[5] L. Jiang, Y. Zhang, C. Li, R. Pang, L. Shi, S. Zhang, J. Hao, Q. Su, Thermoluminescence characteristics of $NaSr_4(BO_3)_3:Ce^{3+}$ under β-ray irradiation, J. Rare Earths 27 (2009) 320–322.
[6] L.H. Jiang, Y.L. Zhang, C.Y. Li, J.Q. Hao, Q. Su, Synthesis, photoluminescence, thermoluminescence and dosimetry properties of novel phosphor $KSr_4(BO_3)_3$:Ce, J. Alloy. Compd. 482 (2009) 313–316.
[7] D. Kouyate, J. Claude, R. Haret, J. Kossanyi, Electroluminescence of Sm^{3+} ions in semiconducting polycrystalline zinc oxide, J. Mater. Chem. 2 (1992) 727–732.
[8] J. Xu, Z. Ju, X. Gao, Y. An, X. Tang, W. Liu, $Na_2CaSn_2Ge_3O_{12}$: a novel host lattice for Sm^{3+}-doped long- persistent phosphorescence materials emitting reddish orange light, Inorg. Chem. 52 (2013) 13875–13881.
[9] J. Zhang, R. Hu, Q. Qin, D. Wang, B. Liu, Y. Wen, M. Zhou, Y. Wang, The origin of two quenching concentrations and unusual afterglow behaviors of $Ba_2SnO_4:Sm^{3+}$ phosphor, J. Lumin. 132 (2012) 2590–2594.
[10] G.R. Dillip, P.M. Kumar, B.D.P. Raju, S.J. Dhoble, Synthesis and luminescence properties of a novel $Na_6CaP_2O_9:Sm^{3+}$ phosphor, J. Lumin. 134 (2013) 333–338.
[11] Z. Xia, D. Chen, Synthesis and luminescence properties of $BaMoO_4:Sm^{3+}$ phosphors, J. Am. Ceram. Soc. 93 (2010) 1397–1401.
[12] L. Wu, Y. Zhang, X.L. Chen, Y.F. Kong, T.Q. Sun, J.J. Xu, Y.P. Xu, The Na_2O–SrO–B_2O_3 diagram in the B-rich part and the crystal structure of $NaSrB_5O_9$, J. Solid State Chem. 180 (2007) 1470–1475.
[13] G.R. Dillip, K. Mallikarjuna, S.J. Dhoble, B.D.P. Raju, The luminescence and structural characteristics of Eu^{3+}-doped $NaSrB_5O_9$ phosphor, J. Phys. Chem. Solids 75 (2014) 8–14.
[14] G.R. Dillip, B. Ramesh, C.M. Reddy, K. Mallikarjuna, O. Ravi, S. J. Dhoble, S.W. Joo, B.D.P. Raju, X-ray analysis and optical studies of Dy^{3+} doped $NaSrB_5O_9$ microstructures for white light generation, J. Alloy. Compd. 615 (2014) 719–727.
[15] W.B. Im, N.N. Fellows, S.P. DenBaars, R. Seshadri, Y.I. Kim, $LaSr_2AlO_5$, a versatile host compound for Ce^{3+}-based yellow phosphors: structural tuning of optical properties and use in solid-state white lighting, Chem. Mater. 21 (2009) 2957–2966.
[16] G.R. Dillip, S.J. Dhoble, B.D.P. Raju, Luminescence properties of $Na_3SrB_5O_{10}:Dy^{3+}$ plate-like microstructures for solid state lighting applications, Opt. Mater. 35 (2013) 2261–2266.
[17] L. Wu, M. Ji, H. Wang, Y. Kong, Y. Zhang, Site occupancy and photoluminescence of Sm^{3+} in $KSr_4(BO_3)_3:Sm^{3+}$ phosphors, Opt. Mater. Express 4 (2014) 1535–1544.
[18] S. Kamimura, H. Yamada, C.N. Xu, Strong reddish-orange light emission from stress-activated $Sr_{n+1}Sn_nO_{3n+1}:Sm^{3+}$ ($n = 1, 2, \infty$) with perovskite-related structures, Appl. Phys. Lett. 101 (2012) 091113–4.
[19] Z. Ju, R. Wei, J. Zheng, X. Gao, S. Zhang, W. Liu, Synthesis and phosphorescence mechanism of a reddish orange emissive long afterglow phosphor Sm^{3+}-doped Ca_2SnO_4, Appl. Phys. Lett. 98 (2011) 121906–3.
[20] P. Klug, L.E. Alexander, X-Ray diffraction procedure, Wiley, New York, 1954.
[21] P. Scardi, M. Leoni, R. Delhez, Line broadening analysis using integral breadth methods: a critical review, J. Appl. Cryst. 37 (2004) 381–390.
[22] V.D. Mote, Y. Purushotham, B.N. Dole, Williamson–Hall analysis in estimation of lattice strain in nanometer-sized ZnO particles, J. Theoretical Appl. Phys. 6 (6) (2012) 1–8.
[23] T.D. Dang, A.N. Banerjee, S.W. Joo, B.K. Min, Synthesis of amourphous and crystalline hollow manganese oxide nanotubes with highly porous walls using carbon nanotube templates and enhanced catalytic activity, Ind. Eng. Chem. Res. 53 (2014) 9743–9753.
[24] R.L. Frost, Y. Xi, R. Scholz, F.M. Belotti, M.C. Filho, Infrared and Raman spectroscopic characterization of the borate mineral colemanite – $CaB_3O_4(OH)_3 \cdot H_2O$ – implications for the molecular structure, J. Mol. Struct. 1037 (2013) 23–28.
[25] C.N. Santos, D.D.S. Meneses, P. Echegut, D.R. Neuville, A. C. Hernandes, A. Ibanez, Structural, dielectric, and optical properties of yttrium calcium borate glasses, Appl. Phys. Lett. 94 (2009) 151901–3.
[26] R.L. Frost, A. López, Y. Xi, L.M. Graça, R. Scholz, A vibrational spectroscopic study of the borate mineral takedaite $Ca_3(BO_3)_2$, Spectrochim. Acta Part A 132 (2014) 833–837.
[27] M.G. Ha, J.H. Lee, J.S. Bae, J.P. Kim, K.S. Hong, H.S. Yang, Photophysical properties of highly efficient red-emitting $CaTiO_3:Eu^{3+}$ phosphors under near ultra-violet excitation, Curr. Appl. Phys. 11 (2011) 1379–1383.
[28] Y.S. Liu, L.T. Zhang, L.F. Cheng, W.B. Yang, Y.D. Xu, Effect of deposition temperature on boron-doped carbon coatings deposited from a BCl_3–C_3H_6–H_2 mixture using low pressure chemical vapor deposition, Appl. Surf. Sci. 255 (2009) 8761–8768.
[29] S.S. Pitale, I.M. Nagpure, V. Kumar, O.M. Ntwaeaborwa, J.J. Terblans, H.C. Swart, Investigations on the low voltage cathodoluminescence stability and surface chemical behaviour using Auger and X-ray photoelectron spectroscopy on $LiSrBO_3:Sm^{3+}$ phosphor, Mater. Res. Bull. 46 (2011) 987–994.
[30] V.V. Atuchin, J.C. Grivel, A.S. Korotkov, Z. Zhang, Electronic parameters of $Sr_2Nb_2O_7$ and chemical bonding, J. Solid State Chem. 181 (2008) 1285–1291.

[31] C.H. Hsieh, H. Jain, A.C. Miller, E.I. Kamitsos, X-ray photoelectron spectroscopy of Al- and B-substituted sodium trisilicate glasses, J. Non-Cryst. Solids 168 (1994) 247–257.
[32] V. Kumar, A.K. Bedyal, S.S. Pitale, O.M. Ntwaeaborwa, H.C. Swart, Synthesis, spectral and surface investigation of $NaSrBO_3$: Sm^{3+} phosphor for full color down conversion in LEDs, J. Alloy. Compd. 554 (2013) 214–220.
[33] K. Granath, M. Bodegard, L. Stolt, The effect of NaF on Cu(In, Ga)Se_2 thin film solar cells, Sol. Energy Mater. Sol. Cells 60 (2000) 279–293.
[34] K. Yoshida, M. Yoshimoto, K. Sasaki, T. Ohnishi, T. Ushiki, J. Hitomi, S. Yamamoto, M. Sigeno, Fabrication of a new substrate for atomic force microscopic observation of DNA molecules from an ultrasmooth sapphire plate, Biophys. J. 74 (1998) 1654–1657.
[35] Q.H. Wu, M. Liu, W. Jaegermann, X-ray photoelectron spectroscopy of $La_{0.5}Sr_{0.5}MnO_3$, Mater. Lett. 59 (2005) 1980–1983.
[36] J. Singh, A. Roychoudhury, M. Srivastava, P.R. Solanki, D.W. Lee, S. H. Lee, B.D. Malhotra, A highly efficient rare earth metal oxide nanorods based platform for aflatoxin detection, J. Mater. Chem. B 1 (2013) 4493–4503.
[37] J. Sun, J. Lai, J. Sun, H. Du, Luminescence properties of a new red emitting Eu^{3+}-doped alkaline-earth fluoborate phosphor: $BaCa_{(1-2x)}BO_3F$:xEu^{3+}, xM^{+} (M=Li, Na, K), J. Rare Earths 29 (2011) 321–325.
[38] H.M. Yang, Z. Wang, M.L. Gong, H. Liang, Luminescence properties of a novel red emitting phosphor, Mg_2GeO_4:Sm^3, J. Alloy. Compd. 488 (2009) 331–333.
[39] L. Đacanin, S.R. Lukic-Petrovic, D.M. Petrovic, M.D. Dramicanin, Photoluminescence of Eu- and Sm-doped $LiInO_2$ phosphor powders, Phys. Scr. 85 (2012) 065703–6.
[40] G. Blasse, Energy transfer between inequivalent Eu^{2+} ions, J. Solid State Chem. 62 (1986) 207–211.
[41] J. Li, J.G. Li, S. Liu, X. Li, X. Sun, Y. Sakka, Greatly enhanced Dy^{3+} emission via efficient energy transfer in gadolinium aluminate garnet ($Gd_3Al_5O_{12}$) stabilized with Lu^3, J. Mater. Chem. C 1 (2013) 7614–7622.
[42] A.K. Parchur, A.I. Prasad, A.A. Ansari, S.B. Rai, R.S. Ningthoujam, Luminescence properties of Tb^{3+}-doped $CaMoO_4$ nanoparticles: annealing effect, polar medium dispersible, polymer film and core–shell formation, Dalton Trans. 41 (2012) 11032–11045.
[43] J. Zheng, Q. Cheng, W. Chen, Z. Guo, C. Chen, Luminescence properties of an orange–red $Ba_5(BO_3)_2(B_2O_5)$:Sm^{3+} phosphor with high color purity, ECS J. Solid State Sci. Technol. 4 (2015) R72–R77.
[44] M.T. Jose, S.R. Anishia, O. Annalakshmi, V. Ramasamy, Determination of thermoluminescence kinetic parameters of thulium doped lithium calcium borate, Radiat. Meas. 46 (2011) 1026–1032.
[45] O. Annalakshmi, M.T. Jose, U. Madhusoodanan, B. Venkatraman, G. Amarendra, Kinetic parameters of lithium tetraborate based TL materials, J. Lumin. 141 (2013) 60–66.
[46] R. Chen, Glow curves with general order kinetics, J. Electrochem. Soc. 116 (1969) 1254–1257.
[47] V.C. Kongre, S.C. Gedam, S.J. Dhoble, Photoluminescence and thermoluminescence characteristics of $BaCa(SO_4)_2$: Ce mixed alkaline earth sulfate, J. Lumin. 135 (2013) 55–59.
[48] B.P. Kore, N.S. Dhoble, S.J. Dhoble, Synthesis and thermoluminescence characterization of $Na_6Mg(SO_4)_4$:RE (RE=Ce, Tb) phosphors, Radiat. Meas. 67 (2014) 35–46.